ADVANCING EARTH AND SPACE SCIENCES

Geophysical Research Letters

RESEARCH LETTER
10.1029/2023GL107731

Energetic Particle Precipitation in Sub-Auroral Polarization Streams

Anton V. Artemyev[1], Ying Zou[2], Xiao-Jia Zhang[1,3], Xing Meng[4], and Vassilis Angelopoulos[1]

[1]University of California, Los Angeles, Los Angeles, CA, USA, [2]Applied Physics Laboratory, Johns Hopkins University, Laurel, MD, USA, [3]Department of Physics, The University of Texas at Dallas, Richardson, TX, USA, [4]Jet Propulsion Laboratory, California Institute of Technology, Pasadena, CA, USA

Key Points:

- Relativistic electron and energetic ion precipitation within sub-auroral polarization streams (SAPS) are reported for DMSP and ELFIN conjunction
- During this event relativistic electron precipitation within SAPS is driven by EMIC waves
- During this event energetic ion precipitation within SAPS is due to field line scattering at the ion isotropy boundary

Supporting Information:

Supporting Information may be found in the online version of this article.

Correspondence to:

A. V. Artemyev,
aartemyev@igpp.ucla.edu

Citation:

Artemyev, A. V., Zou, Y., Zhang, X.-J., Meng, X., & Angelopoulos, V. (2024). Energetic particle precipitation in sub-auroral polarization streams. *Geophysical Research Letters*, *51*, e2023GL107731. https://doi.org/10.1029/2023GL107731

Received 6 DEC 2023
Accepted 8 FEB 2024

Abstract

Sub-auroral polarization streams (SAPS) are one of the most intense manifestations of magnetosphere-ionosphere coupling. Magnetospheric energy transport to the ionosphere within SAPS is associated with Poynting flux and the precipitation of thermal energy (0.03–30 keV) plasma sheet particles. However, much less is known about the precipitation of high-energy (≥50 keV) ions and electrons and their contribution to the low-altitude SAPS physics. This study examines precipitation within one SAPS event using a combination of equatorial THEMIS and low-altitude DMSP and ELFIN observations, which, jointly, cover from a few eV up to a few MeV energy range. Observed SAPS are embedding the ion isotropy boundary, which includes strong 300–1,000 keV ion precipitation. SAPS are associated with intense precipitation of relativistic electrons (≲3 MeV), well equatorward of the electron isotropy boundary. Such relativistic electron precipitation is likely due to electron scattering by electromagnetic ion cyclotron waves at the equator.

Plain Language Summary

Magnetosphere-ionosphere coupling and dynamics are modified by precipitating ion and electron energy fluxes that alter the ionosphere's characteristics. Sub-auroral polarization streams (SAPS) are a classical example of this coupling, encompassing precipitation of plasma sheet (<30 keV) particles, intensification of field-aligned currents, and ionospheric feedback in the form of enhanced electric fields. This study demonstrates, for the first time, that SAPS are associated with precipitation of energetic ions (50–1,000 keV) and relativistic (up to a few MeV) electrons. The 50–1,000 keV ions may dominate the precipitating energy flux at low latitudes, where scattering of plasmasheet ions is significantly reduced. Relativistic electron precipitation significantly extends ionization enhancement effects to altitudes below 100 km, where these electrons deposit their energy.

1. Introduction

Sub-auroral polarization streams (SAPS), and their more intense counterpart, sub-auroral ion drifts (SAID), are often associated with the earthward transport (e.g., substorm injections or enhanced convection) of hot ions, their decoupling from electron motion due to diamagnetic drifts, and the formation of strong polarization electric fields and ionospheric flows (see the review by Mishin & Streltsov, 2021; Yu et al., 2022, and references therein). SAPS/SAID are formed between the inner edge of electron and ion plasma sheet (Anderson et al., 1993; Brandt et al., 2008), close to the plasmapause (see low-altitude and equatorial statistical observations of SAPS/SAID, in He et al., 2014; Nishimura et al., 2022). The magnetosphere-ionosphere connection within SAPS/SAID is provided by ring current (≲30 keV) ion precipitation and field-aligned currents (Burke & Lai, 2021; Figueiredo et al., 2004; W. Wang et al., 2021), which may be part of the substorm current wedge system (Mishin et al., 2017; Z. Wang et al., 2019). Strong polarization electric fields within SAPS/SAID are responsible for the equatorial and ionospheric plasma azimuthal drifts (Foster & Burke, 2002; Galperin et al., 1974; Puhl-Quinn et al., 2007; Spiro et al., 1979). Such fields are subject to filamentation into small-scales (likely due to kinetic Alfven wave generation, see Streltsov & Mishin, 2020). The resultant finite field-aligned electric field component of these waves is responsible for the formation of field-aligned electron streams (Damiano et al., 2016; Hull et al., 2022; Shiokawa et al., 1999). The strong plasma flows and precipitation of ring current ions and plasma sheet electrons (<30 keV) result in ionospheric plasma heating (Moffett et al., 1998; Sheng et al., 2019, 2021) and large-scale density perturbations (Deng et al., 2019; Foster, 2008; Lyons et al., 2021). These SAPS/SAID characteristics are co-located with the middle latitude ionosphere trough (MIT, see Vo & Foster, 2001; Rodger, 2008), or its equatorward edge (e.g., Kunduri et al., 2021; Mishin, 2013).

Although the magnetosphere-ionosphere coupling within SAPS/SAID is mostly attributed to the precipitation of $\lesssim$30 keV particles (plasma sheet electrons and low-energy ring current ions; see, e.g., Mishin and Streltsov (2021); Mishin (2023) and references therein), the physics of SAPS/SAID at the equatorial magnetosphere likely involves the dynamics of energetic (>50 keV) particles. A strong electric field around SAPS/SAID can cause 50–200 keV electron injections deep into the plasmapshere (Califf et al., 2022; Lejosne et al., 2018), whereas nonlinear instabilities (i.e., wave-wave interaction processes, see Main & Sotnikov, 2020) of SAPS/SAID electric fields can lead to the generation of hiss-like whistler-mode waves (Mishin & Sotnikov, 2017). These waves can scatter and precipitate energetic electrons to the ionosphere (Mishin et al., 2011, 2019) affecting the low-altitude ionosphere conductance (see discussion in Liang et al., 2022; Lin et al., 2021; Yu et al., 2018). Under extreme geomagnetic conditions, the inward motion of the plasmapause (the preferred region of SAPS/SAID) may cause SAPS/SAID to intensify VLF-transmitter whistler-mode waves, which can effectively scatter energetic electrons (the so-called concept of impenetrable barrier, see Foster et al., 2016). Furthermore, unlike the strongly magnetized electrons, energetic ions can be scattered by the magnetic field line curvature even within the outer radiation belt (quite close to the plasmapause). These scattered ions can then contribute to the energy flux precipitating into the SAPS region. To date, studies of energetic (>50 keV) particle precipitation into the low-altitude (ionosphere) within SAPS/SAID are very limited. This stems, in part, from the lack of energetic particle measurements on low-altitude satellites capable of measuring plasma flows, such as the Defense Meteorological Satellite Program (DMSP; see Greenspan et al., 1986; Hardy et al., 1984; Rich & Hairston, 1994) and Swarm (Friis-Christensen et al., 2008), the main observational data sets for SAPS/SAID investigations.

Energetic particle precipitation may significantly alter the physics of magnetosphere-ionosphere coupling within SAPS. Relativistic electrons will extend the altitude range of ionization enhancement to <100 km (see Miyoshi et al., 2021; Oyama et al., 2017), while energetic ion precipitation will extend its latitudinal range. In this paper, we study energetic particle precipitation during SAPS using observations from the low-altitude ELFIN CubeSats (Angelopoulos et al., 2020, 2023). ELFIN measures 50–6,000 keV ion and electron fluxes with high pitch-angle and energy resolution. We combine those with low energy measurements from DMSP also at low altitude and with low- and high-energy measurements from the near-equatorial THEMIS satellites (Angelopoulos, 2008). We thus can investigate the full energy range of ion and electron precipitation along the entire flux-tube connected to SAPS/SAID. The selected event contains a combination of ELFIN energetic electron and ion (available only in the 2022 tail season) measurements accompanied by DMSP and near-equatorial THEMIS measurements. Although this is not the only SAPS event captured by ELFIN, but it is a rather fortuitous one that has ion data available during the ELFIN/DMSP conjunction.

2. Spacecraft Observations

We examine the 6-hour interval, 17:00-23:00 UT on 2022-08-07, which includes near-equatorial THEMIS observations of the inner magnetosphere and the near-Earth plasma sheet, two crossings of the nightside *MLT* sector by ELFIN B and three crossings by DMSP-16&17. Ancillary, GOES-16 equatorial observations were also available at this time. Figure 1 shows an overview of the equatorial measurements. The event occurred during a moderate storm ($Sym-H < -50$ nT, $AE > 300$ nT) with one strong AE intensification ($AE \sim 1000$ nT) around 21:30 UT, likely a substorm. THEMIS E crossed the pre-midnight ($MLT \sim 22$) plasmapause around 18:30 UT, as seen from the plasma density profile derived from the spacecraft potential (see Bonnell et al., 2008; Nishimura et al., 2013). It also detected clear equatorial signatures of SAPS (see for details Nishimura et al., 2022): dispersive plasma sheet ion structure with higher energies penetrating deeper into the plasmasphere and strong gradient of plasma sheet electron fluxes (measured by ion and electron electrostatic analyzers at <30 keV, see McFadden et al., 2008). The THEMIS electric field instrument (Bonnell et al., 2008; Cully et al., 2008) detected whistler-mode hiss waves at the earthward side of this region (before 18:00 UT) and bursts of broadband electromagnetic (also detected by the search-coil magnetometer; Le Contel et al., 2008) waves on the tailward side. The latter are likely kinetic-Alfven waves accompanying plasma sheet injections (see Chaston et al., 2012, 2015; Malaspina et al., 2014). In the near-Earth plasma sheet, THEMIS E observed several nearly dispersionless injections (increases of energetic electron fluxes) measured by the solid-state detector (Angelopoulos et al., 2008), marked by the vertical dashed lines at ~20:30, 20:45, 21:00, 21:45, and 22:10 UT. They were associated with magnetic field dipolarizations ($|B_x|$ decreases and B_z increases), as measured by the fluxgate magnetometer, see Auster et al. (2008)). The injections were accompanied by

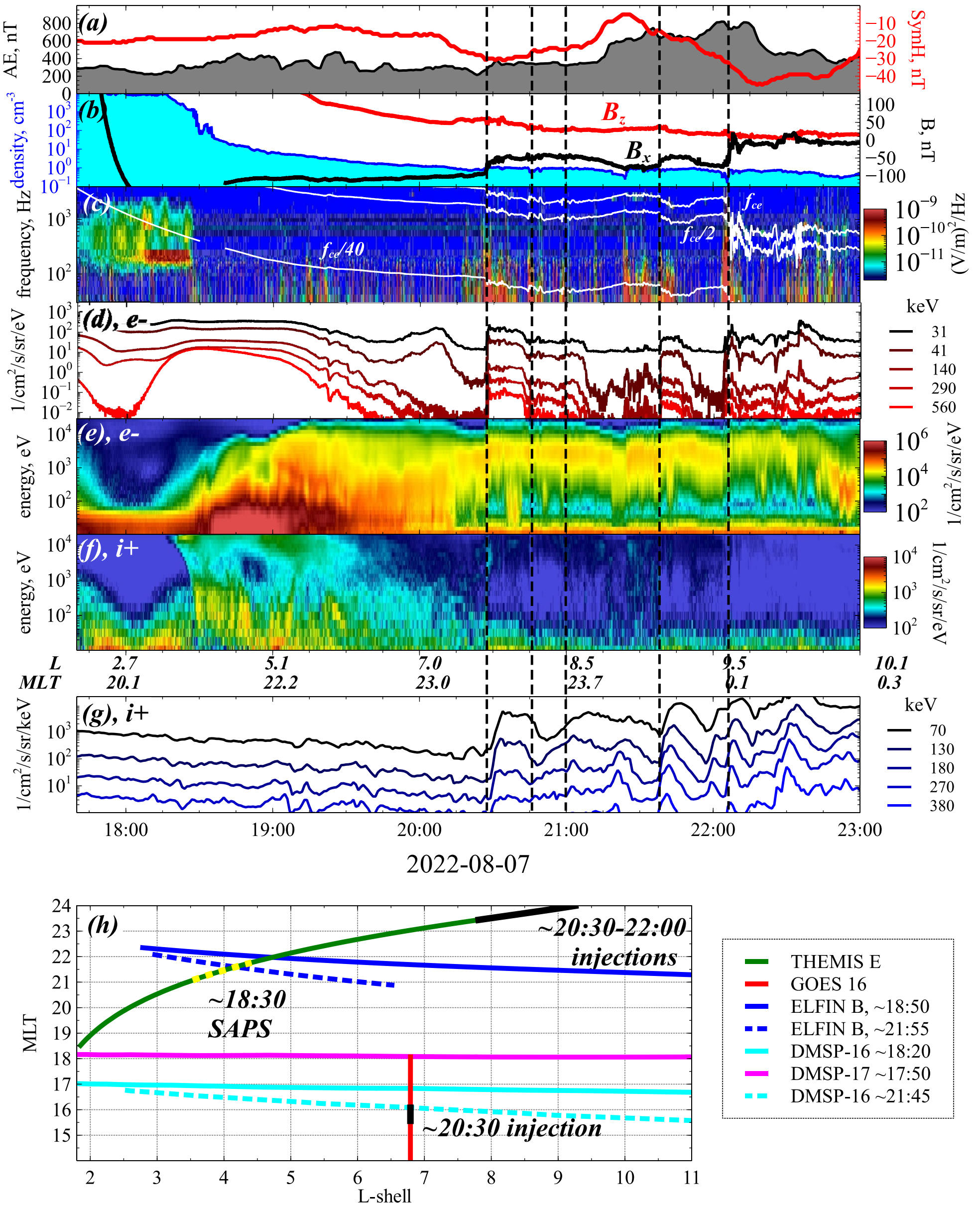

Figure 1. Overview of equatorial (THEMIS E and GOES-16) measurements during a SAPS event: (a) AE and Sym-H geomagnetic indexes, (b) two magnetic field components and plasma density from THEMIS spacecraft potential, (c) wave electric field within the 30–4,000 Hz frequency range (white curves show electron cyclotron frequency, f_{ce}, and $f_{ce}/2$, $f_{ce}/40$), omnidirectional electron fluxes from (d) THEMIS SST and (e) ESA (<30 keV), (f) omnidirectional ion fluxes from THEMIS ESA (<30 keV), (g) GOES-16 energetic proton fluxes, (h) projections of THEMIS E, GOES-16, ELFIN B, and DMSP-16,17 orbits to the equator.

~100 km/s plasma flows (not shown), measured by the THEMIS electrostatic analyzer (McFadden et al., 2008). The first injection, at ~20:30 UT, was detected ~8 min later at GOES-16, at geostationary orbit, (by its space weather suite of instruments, see Dichter et al., 2015; Boudouridis et al., 2020). Therefore, this event displays all the elements of equatorial plasma dynamics that usually accompany SAPS (see, e.g., Mishin & Streltsov, 2021, and references therein). Note that similar, active-time ($AE \sim 1000$ nT) dispersive plasma sheet ion structures, typical of SAPS were also observed by the ERG spacecraft (Miyoshi et al., 2017, 2018) at ~17:30 UT ($MLT \sim 19$) and at ~15:00 UT ($MLT \sim 14.5$). They too occurred near (though, after) a series of strong injections seen at both ERG and GOES-16 around 14:00–15:00 UT (not shown). In other words, this SAPS event lasted several hours and exhibited a significant MLT extent (14.5–22).

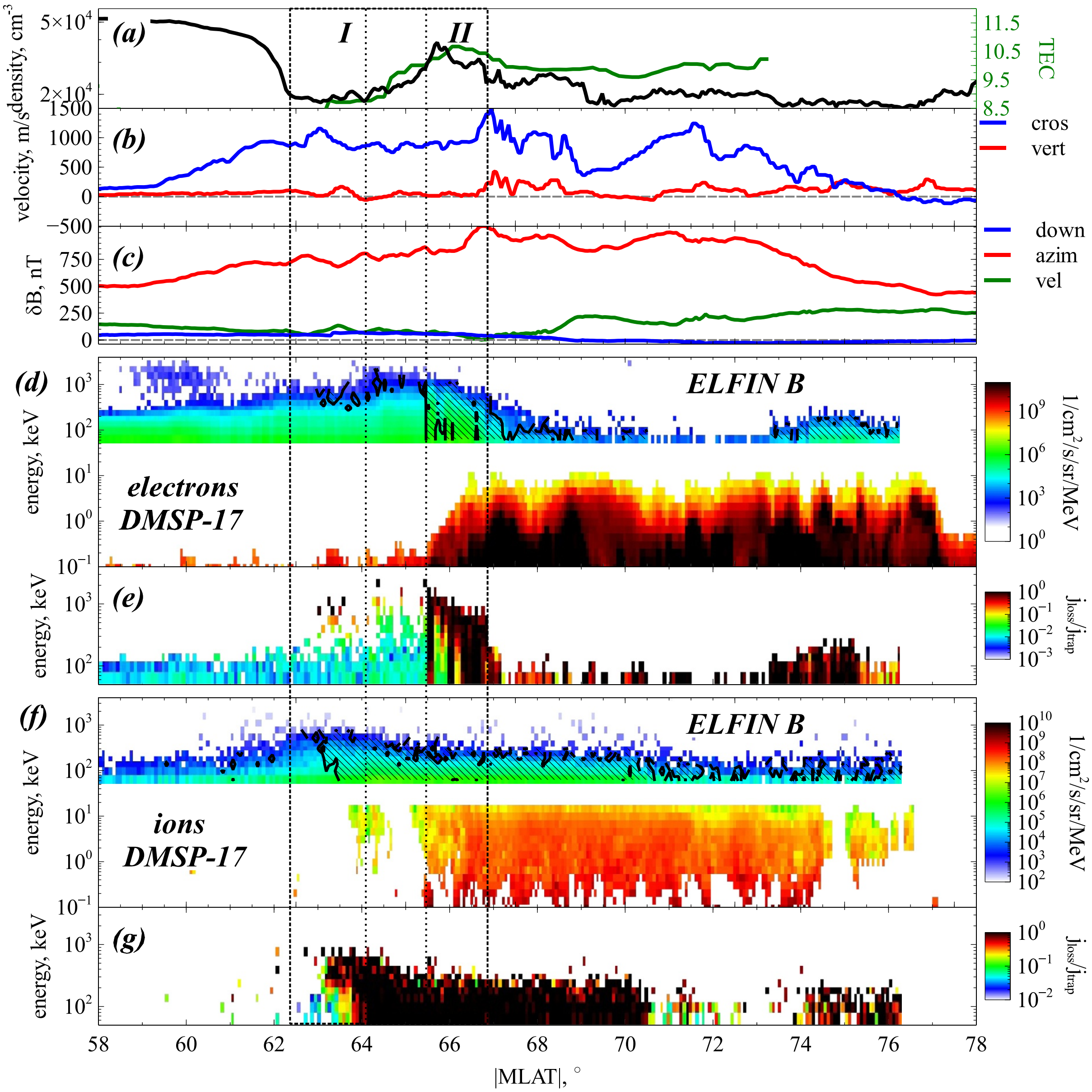

Figure 2. Comparison of ELFIN B (around 18:50 UT) and DMSP-17 (around 17:50 UT) measurements during the same events in Figure 1: (a) DMSP plasma density and TEC along the ELFIN orbit, (b, c) components of plasma drift and magnetic field perturbations measured by DMSP, (d) comparison of locally trapped energetic electron fluxes (from ELFIN) and <30 keV precipitating electron fluxes (from DMSP), (e) precipitating-to-trapped electron flux ratio at ELFIN, (f) comparison of locally trapped energetic ion fluxes (from ELFIN) and <30 keV precipitating ion fluxes (from DMSP), (g) precipitating-to-trapped ion flux ratio at ELFIN. Striped regions in panels (d, f) mark those with precipitating-to-trapped flux ratios above 0.5. The boundary of these regions is shown by the solid black contour.

We then examined ELFIN B crossings at the nightside, with one around 18:50 UT (near the THEMIS E encounter of the equatorial signature of SAPS) and another at ~21:55 UT (after the strong substorm injection). We also examined three DMSP pre-midnight oval crossings, at 17:50, 18:20, and 22:45 UT. Figure 2 shows the first ELFIN B/DMSP-17 orbit. Strong cross-field ion drift (b), characteristic of SAPS, is seen over a large latitudinal range, 60–72°, including the MIT region with density depletion at 62–65° (Figure 2a), within the region 2 (R2) current system ($\delta B_{azim}/\delta MLAT > 0$ (Figure 2c). Note that ELFIN B and DMSP-17 are in opposite hemispheres, which may introduce mapping uncertainties from one to the other (Laundal et al., 2017; Ohma et al., 2018). To compare the two, we employ the one-dimensional profile of the total electron content (TEC) measurements within ±2° in longitude around the ELFIN orbit (see Figure S1 in Supporting Information S1 for the ELFIN projection to the TEC map) and match it with the density measured by DMSP. After shifting ELFIN by $\Delta MLAT \approx 1.5°$, the

TEC maximum at ∼66° and the equatorward TEC decrease (associated with MIT region, see Vo & Foster, 2001; Yizengaw & Moldwin, 2005) coincide with the plasma density maximum at ∼66° and the equatorward minimum as measured by DMSP-17 (see Figure 2a). Although TEC represents the receiver-satellite path-integrated electron density and cannot be quantitatively compared with the locally measured plasma density, the similarity between the TEC along the ELFIN orbit and the in-situ plasma density profiles measured by DMSP-17 validates our further comparison of *MLAT* profiles between DMSP and ELFIN measurements. The shift of $\Delta MLAT \approx 1.5°$ is confirmed by an ELFIN and POES/MetOp energetic particle data comparison (see discussion below).

Figures 2d and 2f show locally trapped (outside the bounce loss-cone) spectra of electrons and ions, respectively. Figures 2e and 2g show the precipitating-to-trapped flux ratios, j_{loss}/j_{trap}, for electrons and ions, respectively. Where these exceed 0.5 the panels above them, (d) and (f) then have been demarcated with striped areas. The ion isotropy boundary, that is, the energy/*L*-shell dispersive feature in the precipitation ratio (see Wilkins et al., 2023, and references therein) is located within $MLAT \in [62.5, 64.0]°$ (also see Ganushkina et al., 2005; Newell et al., 1998; Nishimura et al., 2020). Energetic ion precipitation is captured in the *MLAT* range of 63–70°, with the ion isotropy boundary at ∼63°. This precipitation is at energies not measured by DMSP-17, but is clearly seen in ELFIN. Precipitating fluxes of <30 keV ions measured by DMSP-17 exhibit weak dispersive features around $MLAT \sim 64.5°$. These are contiguous to the low energy portion of the ion isotropy boundary at ELFIN B. However, the dominant precipitation of <30 keV ions occurs within the ion plasma sheet, seen at DMSP at $MLAT > 65°$ (Figure 2f).

The electron isotropy boundary ($MLAT \in [65.5, 66.5]°$) is located 1.5°–3.0° poleward of the ion isotropy boundary, as expected (e.g., Sergeev et al., 1993; Sergeev et al., 2012). Nevertheless, both ion and electron isotropy boundaries still fall within a region characterized by strong ionospheric ion drifts (>500 m/s, Figure 2b) and in the R2 current system ($\delta B_{zim}/\delta MLAT > 0$, Figure 2c). Figure S2 in Supporting Information S1 shows the location of ion and electron isotropy boundaries detected by several POES/MetOp satellites, close (in *MLT*) to the DMSP-17 orbit: between 18:10-18:30 UT, POES 15, 18, and 19 detected the ion isotropy boundary at $MLT \in [19, 20]$ around $MLAT \in [62°, 63°]$, whereas POES 19 also detected the electron isotropy boundary around $MLAT \sim 66°$. The *MLATs* of these boundaries coincide with those detected by ELFIN, validating the comparison of latitudinal profiles between ELFIN B and DMSP-17 measurements.

DMSP-17 observed precipitation of plasma sheet electrons with energies <10 keV and ions with energies <30 keV poleward of the ELFIN-B electron isotropy boundary. Electron isotropy boundary and the weak precipitation of relativistic electrons captured by ELFIN at $MLAT \in [62.5°, 64°]$ (Figure 2e) is roughly located around the MIT region, within the uncertainty level of ELFIN and DMSP *MLAT* profile comparison (note that this uncertainty is at least about $\Delta MLAT = 1.5°$, which is used to match the DMSP density profile and the TEC profile along the ELFIN orbit). This is a transition region between the ion plasma sheet at $MLAT > 64°$, and the ring current region characterized by >300 keV ion fluxes. The precipitation of relativistic electrons is likely caused by the near-equatorial electron resonance with electromagnetic ion cyclotron (EMIC) waves (see, e.g., Angelopoulos et al., 2023; Capannolo et al., 2022; Grach et al., 2022; A. G. Yahnin et al., 2016). Generation of EMIC waves requires transverse ion anisotropy, that is, lower field-aligned fluxes in comparison with equatorial (90°) fluxes (Chen et al., 2009, and references therein). Indeed, DMSP observations show low fluxes of (precipitating) <30 keV ions within the region of relativistic electron precipitation, that can be explained insufficiently strong ion scattering at the equator resulted in lower field-aligned fluxes. This also holds true for <200 keV ions measured by ELFIN at $MLAT < 64°$ (equatorward of the isotropy boundary). In other words, ions at these energies may also exhibit strong transverse anisotropy and contribute to EMIC wave generation. Figure 2 demonstrates that the SAPS (and likely also MIT) includes the [50,500] keV ion isotropy boundary (region I), the electron isotropy boundary (region II), and bursts of relativistic (>500 keV) electron precipitation, which are likely driven by EMIC wave scattering.

During this event, DMSP-16 was also in close proximity to ELFIN's orbit in time. However, it was situated slightly farther away in *MLT* (duskward) from DMSP-17 (see Figure 1h). The main difference between DMSP-16 and DMSP-17 observations is that the dispersive <30 keV ion precipitation burst at DMSP-16 (but not at DMSP-17) occurred right around the ion isotropy boundary captured by ELFIN B. That is at $MLAT \sim 62.5°$ in region I (refer to Figure S3 in Supporting Information S1). Other ionospheric signatures of SAPS are consistent between DMSP-16 and DMSP-17. This suggests that this SAPS event persists for a long time (hours), justifying our comparison of DMSP-17 data at ∼17:50 UT with ELFIN B at ∼18:50 UT.

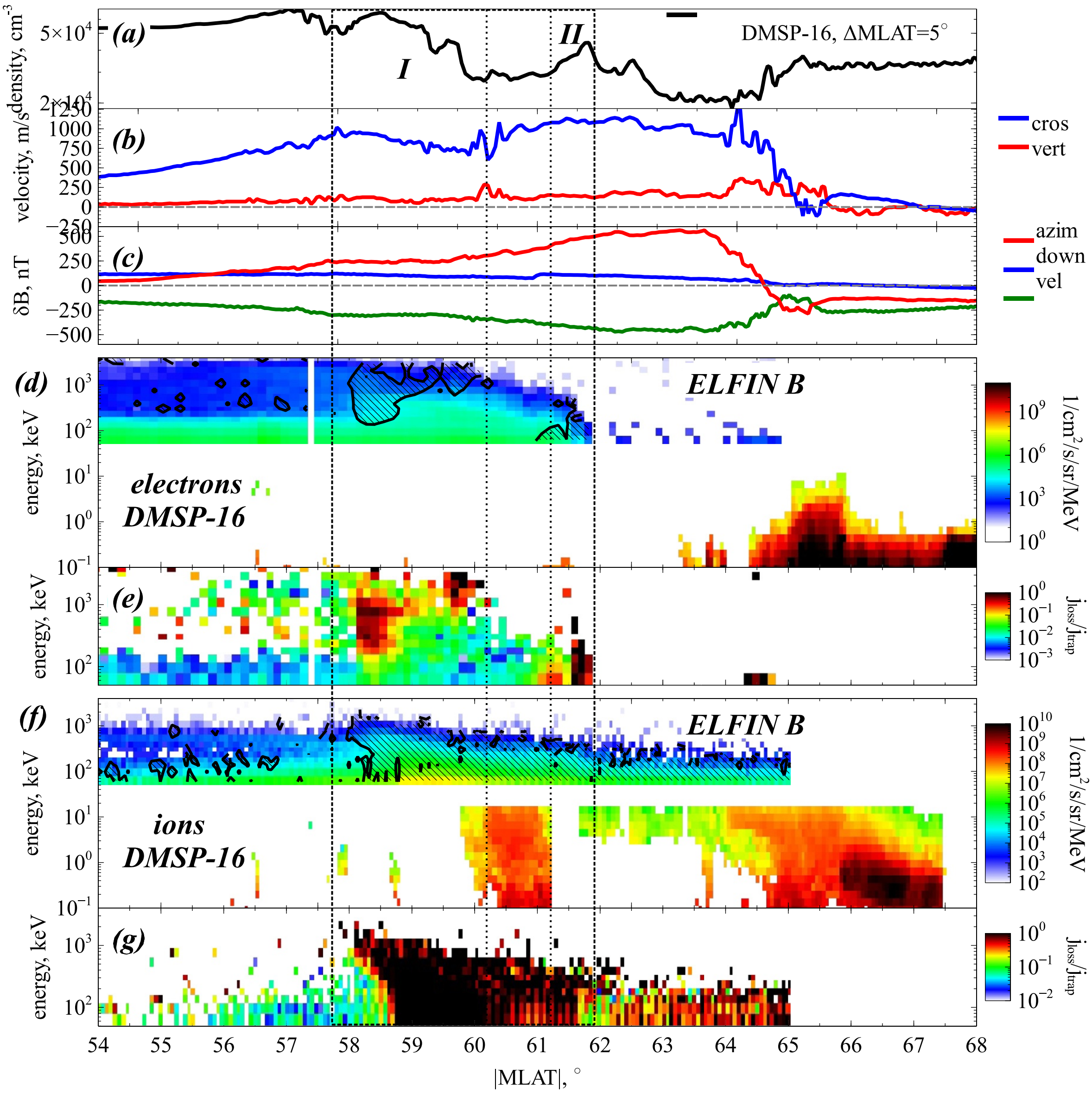

Figure 3. Comparison of ELFIN B (around 21:55 UT) and DMSP-16 (around 21:45 UT) measurements: (a) DMSP plasma density, (b, c) components of plasma drift and magnetic field perturbations measured by DMSP, (d) comparison of locally trapped energetic electron fluxes (from ELFIN) and <30 keV precipitating electron fluxes (from DMSP), (e) precipitating-to-trapped electron flux ratio at ELFIN, (f) comparison of locally trapped energetic ion fluxes (from ELFIN) and <30 keV precipitating ion fluxes (from DMSP), (g) precipitating-to-trapped ion flux ratio at ELFIN. Striped regions in panels (d, f) mark those with precipitating-to-trapped flux ratios above 0.1. The boundary of these regions is shown by the solid black contour. Note that during this event, TEC data along the ELFIN orbit are fragmentary, so we cannot infer the TEC profile along ELFIN orbit in panel (a).

Interestingly, Figure 2 does not show any sub-relativistic (<500 keV) electron precipitation equatorward from the electron isotropy boundary, within SAPS (as expected from electron scattering by whistler-mode waves, see Mishin et al., 2011; Mishin & Sotnikov, 2017). Instead, it reveals weak relativistic electron precipitation likely driven by EMIC waves. Such precipitation can be enhanced after a series of strong ion injections, as observed by GOES-16 between 20:30 UT and 22:00 UT (see Figure 1f). This is because these injections bring in hot, anisotropic ions to drive the EMIC waves (e.g., Chen et al., 2010; Jun et al., 2019). Figure 3 shows the second ELFIN B orbit crossing the nightside magnetosphere at ∼22:00 UT, in the aftermath of these injections. As shown in Figure S3 in Supporting Information S1, there is a $\Delta MLAT = 4°$ shift between DMSP-16 and DMSP-17 latitudinal profiles. Figure 2a shows a good agreement in density/TEC profiles between DMSP-17 and ELFIN B. To match the density peak (as seen by both DMSP-16, 17) and the electron isotropy boundary at ELFIN B (as in Figure 2), we shift DMSP-16 latitudinal profiles by $\Delta MLAT = 5°$ (which is also consistent with the relative $MLAT$ shift between DMSP-16 and DMSP-17; see Figure S3 in Supporting Information S1). Note that this shift also set a scale of $\Delta MLAT$ uncertainty of ELFIN and DMSP comparison.

As shown in Figure 3, the electron isotropy boundary is not that evident at ELFIN measurements, but there are isotropic electron (<200 keV) precipitation at the earthward (inner edge) edge of the electron plasma sheet (region II). ELFIN did not detect the low-altitude projection of the energetic electron plasma sheet (DMSP-16 detected <1 keV plasma sheet electrons at $MLAT > 65°$), because it occurred during the late stage of the magnetotail current sheet thinning (see the $|B_x|$ increase before 22:10 UT in Figure 1b), when the near-Earth plasma sheet filled by energetic electrons is projected to a quite narrow latitudinal region, $\Delta MLAT \sim 1°$, at low altitudes (see details in Artemyev et al., 2022).

Similar to Figure 2, the ion isotropy boundary at ELFIN B (region I, $MLAT \in [58, 59°]$) in Figure 3 is within the SAPS region characterized by the large ion drift flow ($MLAT < 64°$). Figure S4 in Supporting Information S1 confirms the locations of ion and electron isotropy boundaries in the MLT sector of DMSP-16: around 21:30-22:10 UT at $MLT \in [19, 21]$, POES 15, 18, 19, and MetOp-1 detected the ion isotropy boundary at $MLAT \in [59, 60]°$. The SAPS also coincides strong precipitation of relativistic (up to 3 MeV) electrons. One such burst is at $MLAT \sim 60°$. ELFIN B captured another large burst of relativistic electron precipitation at $MLAT \sim 58°$, right in the middle of the SAPS. This burst is accompanied by sub-relativistic precipitation, which might be driven by whistler-mode waves. However, the main attribute of whistler-driven precipitation is the maximum precipitating fluxes (and precipitating-to-trapped flux ratio) at the lowest energy channels (50–100 keV), because the whistler-mode diffusion rate is maximizes at energies below 100 keV (see Tsai et al., 2022; Zhang et al., 2022, 2023, for discussion and data/model comparison for whistler-driven precipitation patterns observed by ELFIN). The sub-relativistic precipitation around $MLAT \sim 58°$ are rather the low-energy tail of relativistic electron precipitation and do not show a peak of precipitating-to-trapped flux ratio at 50–100 keV. This precipitation pattern is reminiscent of EMIC-driven precipitation with contributions from high-frequency EMIC wave spectra (Angelopoulos et al., 2023) and nonresonant effects (An et al., 2022). An additional feature of this precipitation pattern is that it locates well equatorward from the isotropic <100 keV electron precipitation from the plasma sheet and shows signatures of energy/L-shell dispersion (contours of constant precipitating-to-trapped flux ratio show an energy increase with L-shell increase within [58.5°, 60°], see panels (d, e)). ELFIN detected multiple such events during strong substorms (see Artemyev et al., 2023, for discussions of the energy/L-shell dispersion in EMIC-driven precipitation), the preferable condition for the SAPS formation, confirming that the event from Figures 2 and 3 is not unique, but rather a typical SAPS-associated electron precipitation pattern.

A summary of the observations in Figures 2 and 3 is shown in Figure 4 (top and bottom panels, respectively), which depicts the density and the integrated energy flux of precipitating electrons ($J_{>50}$ keV, $J_{>500}$ keV) and of precipitating ions ($J_{>50}$ keV). Poleward of the electron isotropy boundary, the density variations can be attributed to plasma sheet (<10 keV) precipitation that heats the polar ionosphere (Moffett et al., 1998; Sheng et al., 2019). However, at sub-auroral latitudes, there only exist energetic electron precipitation bursts driven by wave-particle interactions and energetic ion precipitation. The latter one may be driven by EMIC waves (e.g., A. Yahnin & Yahnina, 2007) and curvature scattering (e.g., Sergeev et al., 2012). Figures 2 and 3 demonstrate strong energy/L-shell dispersion of energetic ion precipitation (at 63° and 58.5°, respectively), the main signature of the curvature scattering effect (e.g., Newell et al., 1998; Sergeev et al., 1993), and thus the ion precipitation poleward from the isotropy boundary is likely driven by the curvature scattering in the plasma sheet. As shown in the integrated precipitating fluxes, the red curve is quite close to the blue one, indicating that the precipitating electron energy fluxes are dominated by relativistic electrons (though still smaller than ion energy fluxes). Within the uncertainty level of ELFIN and DMSP latitudinal profiles, the electron precipitation within the electron isotropy boundary (as shown in Figure 2) and electron precipitation due to EMIC waves (as shown in Figure 3) are well inside the SAPS region, and likely also inside MIT region (see Figure 4). Precipitating relativistic electrons deposit most of their energy in the lower (below 80 km) ionosphere (in the D-region and below, see, e.g., Pettit et al., 2023; Xu et al., 2020). Thus, they cannot directly affect the F/E-regions where SAPS are formed (e.g., Mishin & Streltsov, 2021; Yu et al., 2022, and references therein). On the other hand, energetic ions, with energy fluxes higher than electron fluxes during this event, will deposit their energy above 100 km, well within the E-region (Fang et al., 2013; Tian et al., 2023). Therefore, observations of such relativistic electron precipitation imply that SAPS

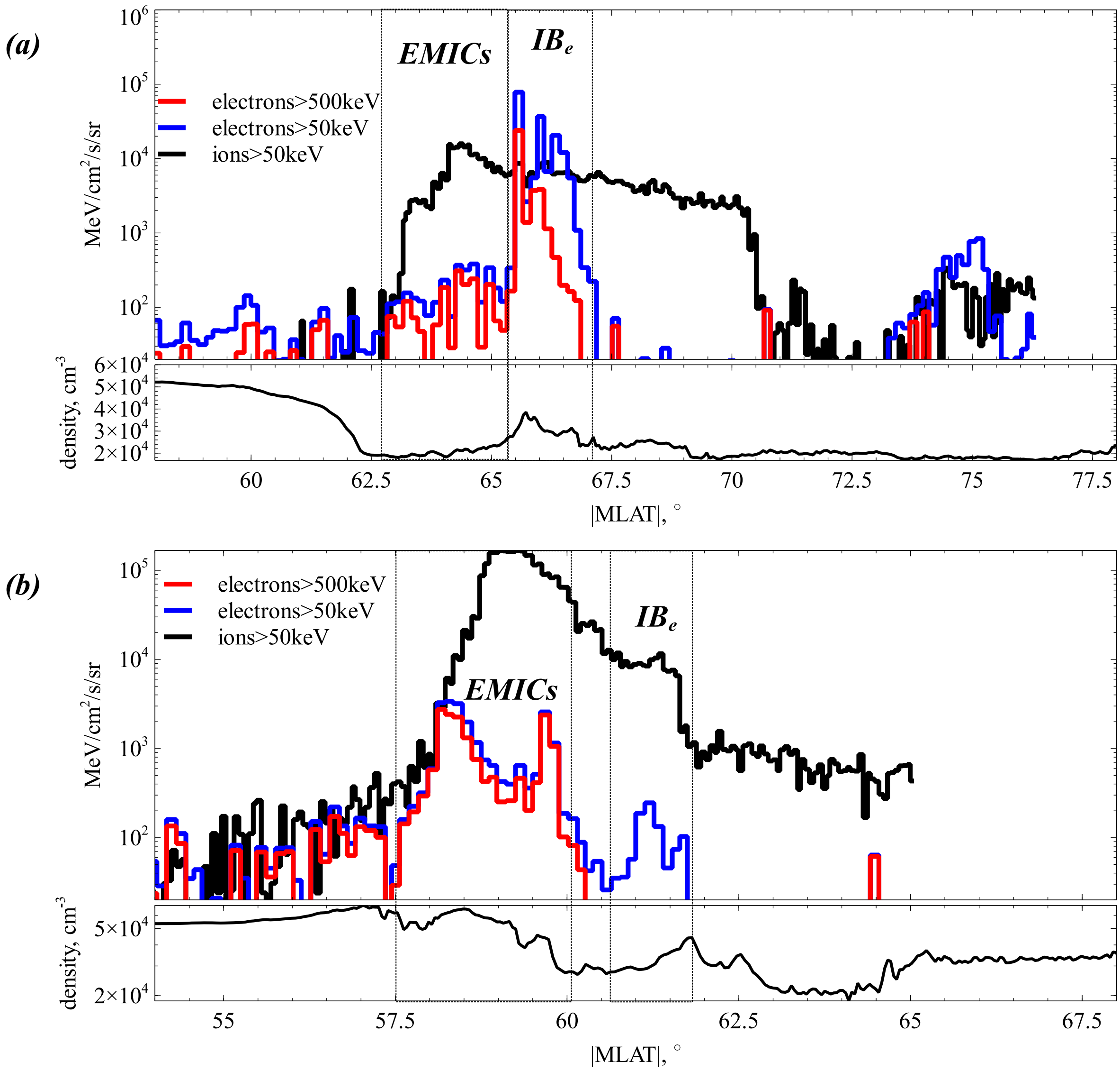

Figure 4. Comparison of the density profile (from DMSP measurements in panels (a) of Figures 2 and 3) and integrated energy flux of precipitating electrons and ions (from ELFIN measurements in panels (d, e) of Figures 2 and 3). Electron isotropy boundary IB_e and EMIC-driven precipitation regions are indicated.

may lead to dynamics in the lower altitude ionosphere, whereas the much more spread energetic ion precipitation which affects conductivity may expand the latitudinal range of SAPS effects.

3. Conclusions

In this study we examined the energetic (up to relativistic energies) electron and ion precipitation within the SAPS region. The comparison of DMSP and ELFIN measurements shows that SAPS includes (is embedded with) strong precipitation of [100,1000] keV ions at the ion isotropy boundary and strong precipitation of ≥100 keV electrons at the electron isotropy boundary. Within the ion isotropy boundary, ELFIN also detected relativistic electron precipitation bursts, likely resulting from electron scattering by EMIC waves. Within the uncertainty level of ELFIN and DMSP latitudinal profiles, [10,1000] keV ion (observed by DMSP and ELFIN) and [100,3000] keV electron precipitation (observed by ELFIN) are likely inside the MIT region.

As also demonstrated in this comparison between DMSP and ELFIN, measurements of energetic electron and ion (>100 keV) can more effectively delineate the edges (the equatorial region with strong curvature scattering) and precipitation bursts (due to wave-particle resonant interactions) than <30 keV particle measurements. The

10.1029/2023GL107731

correlation between relativistic electron precipitation and SAPS highlights the importance of mesoscale transients, such as plasma sheet injections contributing to SAPS formation, in the energy input into the lower ionosphere (D-region, ≤80 km) and magnetosphere-ionosphere coupling (see also discussions in Heelis & Maute, 2020; Huang, 2021).

Data Availability Statement

Fluxes measured by ELFIN are available in the ELFIN data archive in CDF format (ELFIN, 2023). Total electron content (TEC) maps are provided by MIT Haystack via the Madrigal database (TEC, 2023); see Rideout and Coster (2006), Coster et al. (2013), and Vierinen et al. (2015). Data analysis was done using SPEDAS V4.1 (Angelopoulos et al., 2019). The software can be downloaded from (SPEDAS, 2023).

Acknowledgments

We are grateful to NASA's CubeSat Launch Initiative for ELFIN's successful launch in the desired orbits. We acknowledge early support of ELFIN project by the AFOSR, under its University Nanosat Program, UNP-8 project, contract FA9453-12-D-0285, and by the California Space Grant program. We acknowledge critical contributions of numerous volunteer ELFIN team student members. A.V.A and X.-J. Z. acknowledge support from the NASA Grants 80NSSC23K0108, 80NSSC23K0403. X.-J. Z. acknowledges support from the NSF Grant 2329897. V. A. acknowledges support from NSF Grants AGS-1242918, AGS-2019950 and NASA contract NAS5-02099. Y. Z. acknowledge support from the NASA Grant 80NSSC21K0729 and NSF AGS-2332311. Part of the research was carried out at the Jet Propulsion Laboratory, California Institute of Technology, under a contract with the National Aeronautics and Space Administration (80NM0018D0004).

References

An, X., Artemyev, A., Angelopoulos, V., Zhang, X., Mourenas, D., & Bortnik, J. (2022). Nonresonant scattering of relativistic electrons by electromagnetic ion cyclotron waves in Earth's radiation belts. *Physical Review Letters*, *129*(13), 135101. https://doi.org/10.1103/PhysRevLett.129.135101

Anderson, P. C., Hanson, W. B., Heelis, R. A., Craven, J. D., Baker, D. N., & Frank, L. A. (1993). A proposed production model of rapid subauroal ion drifts and their relationship to substorm evolution. *Journal of Geophysical Research*, *98*(A4), 6069–6078. https://doi.org/10.1029/92JA01975

Angelopoulos, V. (2008). The THEMIS mission. *Space Science Reviews*, *141*(1–4), 5–34. https://doi.org/10.1007/s11214-008-9336-1

Angelopoulos, V., Cruce, P., Drozdov, A., Grimes, E. W., Hatzigeorgiu, N., King, D. A., et al. (2019). The space physics environment data analysis system (SPEDAS). *Space Science Reviews*, *215*(1), 9. https://doi.org/10.1007/s11214-018-0576-4

Angelopoulos, V., McFadden, J. P., Larson, D., Carlson, C. W., Mende, S. B., Frey, H., et al. (2008). Tail reconnection triggering substorm onset. *Science*, *321*(5891), 931–935. https://doi.org/10.1126/science.1160495

Angelopoulos, V., Tsai, E., Bingley, L., Shaffer, C., Turner, D. L., Runov, A., et al. (2020). The ELFIN mission. *Space Science Reviews*, *216*(5), 103. https://doi.org/10.1007/s11214-020-00721-7

Angelopoulos, V., Zhang, X. J., Artemyev, A. V., Mourenas, D., Tsai, E., Wilkins, C., et al. (2023). Energetic electron precipitation driven by electromagnetic ion cyclotron waves from ELFIN's low altitude perspective. *Space Science Reviews*, *219*(5), 37. https://doi.org/10.1007/s11214-023-00984-w

Artemyev, A. V., Angelopoulos, V., Zhang, X.-J., Chen, L., & Runov, A. (2023). Dispersed relativistic electron precipitation patterns between the ion and electron isotropy boundaries. *Journal of Geophysical Research: Space Physics*, *128*(12), e2023JA032200. https://doi.org/10.1029/2023JA032200

Artemyev, A. V., Angelopoulos, V., Zhang, X. J., Runov, A., Petrukovich, A., Nakamura, R., et al. (2022). Thinning of the magnetotail current sheet inferred from low-altitude observations of energetic electrons. *Journal of Geophysical Research: Space Physics*, *127*(10), e2022JA030705. https://doi.org/10.1029/2022JA030705

Auster, H. U., Glassmeier, K. H., Magnes, W., Aydogar, O., Baumjohann, W., Constantinescu, D., et al. (2008). The THEMIS fluxgate magnetometer. *Space Science Reviews*, *141*(1–4), 235–264. https://doi.org/10.1007/s11214-008-9365-9

Bonnell, J. W., Mozer, F. S., Delory, G. T., Hull, A. J., Ergun, R. E., Cully, C. M., et al. (2008). The electric field instrument (EFI) for THEMIS. *Space Science Reviews*, *141*(1–4), 303–341. https://doi.org/10.1007/s11214-008-9469-2

Boudouridis, A., Rodriguez, J. V., Kress, B. T., Dichter, B. K., & Onsager, T. G. (2020). Development of a Bowtie inversion technique for real-time processing of the GOES-16/-17 SEISS MPS-HI electron channels. *Space Weather*, *18*(4), e02403. https://doi.org/10.1029/2019SW002403

Brandt, P. C., Zheng, Y., Sotirelis, T. S., Oksavik, K., & Rich, F. J. (2008). The linkage between the ring current and the ionosphere system. *Washington DC American Geophysical Union Geophysical Monograph Series*, *181*, 135–143. https://doi.org/10.1029/181GM13

Burke, W. J., & Lai, P.-C. (2021). Early main-phase electrodynamics of the ring current inferred from DMSP. *Journal of Atmospheric and Solar-Terrestrial Physics*, *213*, 105523. https://doi.org/10.1016/j.jastp.2020.105523

Califf, S., Zhao, H., Gkioulidou, M., Manweiler, J. W., Mitchell, D. G., & Tian, S. (2022). Multi-event study on the connection between subauroral polarization streams and deep energetic particle injections in the inner magnetosphere. *Journal of Geophysical Research: Space Physics*, *127*(2), e2021JA029895. https://doi.org/10.1029/2021JA029895

Capannolo, L., Li, W., Millan, R., Smith, D., Sivadas, N., Sample, J., & Shekhar, S. (2022). Relativistic electron precipitation near midnight: Drivers, distribution, and properties. *Journal of Geophysical Research: Space Physics*, *127*(1), e30111. https://doi.org/10.1029/2021JA030111

Chaston, C. C., Bonnell, J. W., Clausen, L., & Angelopoulos, V. (2012). Energy transport by kinetic-scale electromagnetic waves in fast plasma sheet flows. *Journal of Geophysical Research*, *117*(A9), 9202. https://doi.org/10.1029/2012JA017863

Chaston, C. C., Bonnell, J. W., Kletzing, C. A., Hospodarsky, G. B., Wygant, J. R., & Smith, C. W. (2015). Broadband low-frequency electromagnetic waves in the inner magnetosphere. *Journal of Geophysical Research*, *120*(10), 8603–8615. https://doi.org/10.1002/2015JA021690

Chen, L., Thorne, R. M., & Horne, R. B. (2009). Simulation of EMIC wave excitation in a model magnetosphere including structured high-density plumes. *Journal of Geophysical Research*, *114*(A7), A07221. https://doi.org/10.1029/2009JA014204

Chen, L., Thorne, R. M., Jordanova, V. K., Wang, C.-P., Gkioulidou, M., Lyons, L., & Horne, R. B. (2010). Global simulation of EMIC wave excitation during the 21 April 2001 storm from coupled RCM-RAM-HOTRAY modeling. *Journal of Geophysical Research*, *115*(A7), A07209. https://doi.org/10.1029/2009JA015075

Coster, A., Williams, J., Weatherwax, A., Rideout, W., & Herne, D. (2013). Accuracy of GPS total electron content: GPS receiver bias temperature dependence. *Radio Science*, *48*(2), 190–196. https://doi.org/10.1002/rds.20011

Cully, C. M., Ergun, R. E., Stevens, K., Nammari, A., & Westfall, J. (2008). The THEMIS digital fields board. *Space Science Reviews*, *141*(1–4), 343–355. https://doi.org/10.1007/s11214-008-9417-1

Damiano, P. A., Johnson, J. R., & Chaston, C. C. (2016). Ion gyroradius effects on particle trapping in kinetic alfvn waves along auroral field lines. *Journal of Geophysical Research*, *121*(11), 10831–10844. https://doi.org/10.1002/2016JA022566

Deng, Y., Heelis, R., Lyons, L. R., Nishimura, Y., & Gabrielse, C. (2019). Impact of flow bursts in the auroral zone on the ionosphere and thermosphere. *Journal of Geophysical Research: Space Physics*, *124*(12), 10459–10467. https://doi.org/10.1029/2019JA026755
Dichter, B. K., Galica, G. E., McGarity, J. O., Tsui, S., Golightly, M. J., Lopate, C., & Connell, J. J. (2015). Specification, design, and calibration of the space weather suite of instruments on the NOAA GOES-R program spacecraft. *IEEE Transactions on Nuclear Science*, *62*(6), 2776–2783. https://doi.org/10.1109/TNS.2015.2477997
ELFIN. (2023). Electron losses and fields investigation (ELFIN) data archive [Dataset]. ELFIN. Retrieved from https://data.elfin.ucla.edu/
Fang, X., Lummerzheim, D., & Jackman, C. H. (2013). Proton impact ionization and a fast calculation method. *Journal of Geophysical Research: Space Physics*, *118*(8), 5369–5378. https://doi.org/10.1002/jgra.50484
Figueiredo, S., Karlsson, T., & Marklund, G. (2004). Investigation of subauroral ion drifts and related field-aligned currents and ionospheric Pedersen conductivity distribution. *Annales Geophysicae*, *22*(3), 923–934. https://doi.org/10.5194/angeo-22-923-2004
Foster, J. C. (2008). Ionospheric-magnetospheric-heliospheric coupling: Storm-time thermal plasma redistribution. *Washington DC American Geophysical Union Geophysical Monograph Series*, *181*, 121–134. https://doi.org/10.1029/181GM12
Foster, J. C., & Burke, W. J. (2002). SAPS: A new categorization for sub-auroral electric fields. *EOS Transactions*, *83*(36), 393–394. https://doi.org/10.1029/2002EO000289
Foster, J. C., Erickson, P. J., Baker, D. N., Jaynes, A. N., Mishin, E. V., Fennel, J. F., et al. (2016). Observations of the impenetrable barrier, the plasmapause, and the VLF bubble during the 17 March 2015 storm. *Journal of Geophysical Research: Space Physics*, *121*(6), 5537–5548. https://doi.org/10.1002/2016JA022509
Friis-Christensen, E., Lühr, H., Knudsen, D., & Haagmans, R. (2008). Swarm an Earth observation mission investigating geospace. *Advances in Space Research*, *41*(1), 210–216. https://doi.org/10.1016/j.asr.2006.10.008
Galperin, Y. I., Ponomarev, V. N., & Zosimova, A. G. (1974). Plasma convection in polar ionosphere. *Annales de Geophysique*, *30*(1), 1–7.
Ganushkina, N. Y., Pulkkinen, T. I., Kubyshkina, M. V., Sergeev, V. A., Lvova, E. A., Yahnina, T. A., & Fritz, T. (2005). Proton isotropy boundaries as measured on mid- and low-altitude satellites. *Annales Geophysicae*, *23*(5), 1839–1847. https://doi.org/10.5194/angeo-23-1839-2005
Grach, V. S., Artemyev, A. V., Demekhov, A. G., Zhang, X.-J., Bortnik, J., Angelopoulos, V., et al. (2022). Relativistic electron precipitation by EMIC waves: Importance of nonlinear resonant effects. *Geophysical Research Letters*, *49*(17), e99994. https://doi.org/10.1029/2022GL099994
Greenspan, M. E., Anderson, P. B., & Pelagatti, J. M. (1986). Characteristics of the thermal plasma monitor (SSIES) for the defense meteorological satellite program (DMSP) spacecraft S 8 through f 10 (Tech. Rep.). Tech. Rep. AFGL-TR-86-0227, Hanscom AFB, Mass. Retrieved from https://apps.dtic.mil/sti/citations/ADA176924
Hardy, D. A., Schmitt, L. K., Gussenhoven, M. S., Marshall, F. J., & Yeh, H. C. (1984). Precipitating electron and ion detectors (SSJ/4) for the block 5D/Flights 6-10 DMSP (Defense Meteorological Satellite Program) satellites: Calibration and data presentation.
He, F., Zhang, X.-X., & Chen, B. (2014). Solar cycle, seasonal, and diurnal variations of subauroral ion drifts: Statistical results. *Journal of Geophysical Research: Space Physics*, *119*(6), 5076–5086. https://doi.org/10.1002/2014JA019807
Heelis, R. A., & Maute, A. (2020). Challenges to understanding the Earth's ionosphere and thermosphere. *Journal of Geophysical Research: Space Physics*, *125*(7), e27497. https://doi.org/10.1029/2019JA027497
Huang, C. (2021). Magnetospheric energy input to the ionosphere. In C. Huang & G. Lu (Eds.), *Ionosphere dynamics and applications* (Vol. 3, p. 3). https://doi.org/10.1002/9781119815617.ch1
Hull, A. J., Damiano, P. A., Chaston, C. C., Johnson, J. R., & Reeves, G. D. (2022). Electron energization signatures in traveling kinetic Alfvén waves at storm time injection fronts. *Geophysical Research Letters*, *49*(15), e99318. https://doi.org/10.1029/2022GL099318
Jun, C. W., Yue, C., Bortnik, J., Lyons, L. R., Nishimura, Y., & Kletzing, C. (2019). EMIC wave properties associated with and without injections in the inner magnetosphere. *Journal of Geophysical Research: Space Physics*, *124*(3), 2029–2045. https://doi.org/10.1029/2018JA026279
Kunduri, B. S. R., Baker, J. B. H., Ruohoniemi, J. M., Coster, A. J., Vines, S. K., Anderson, B. J., et al. (2021). An examination of magnetosphere-ionosphere influences during a SAPS event. *Geophysical Research Letters*, *48*(19), e95751. https://doi.org/10.1029/2021GL095751
Laundal, K. M., Cnossen, I., Milan, S. E., Haaland, S. E., Coxon, J., Pedatella, N. M., et al. (2017). North-South asymmetries in Earth's magnetic field. Effects on high-latitude geospace. *Space Science Reviews*, *206*(1–4), 225–257. https://doi.org/10.1007/s11214-016-0273-0
Le Contel, O., Roux, A., Robert, P., Coillot, C., Bouabdellah, A., de La Porte, B., et al. (2008). First results of the THEMIS search coil magnetometers. *Space Science Reviews*, *141*(1–4), 509–534. https://doi.org/10.1007/s11214-008-9371-y
Lejosne, S., Kunduri, B. S. R., Mozer, F. S., & Turner, D. L. (2018). Energetic electron injections deep into the inner magnetosphere: A result of the subauroral polarization stream (SAPS) potential drop. *Geophysical Research Letters*, *45*(9), 3811–3819. https://doi.org/10.1029/2018GL077969
Liang, J., St-Maurice, J. P., & Donovan, E. F. (2022). Model simulation of SAID intensification in the ionosphere under a current generator: The role of ion Pedersen transport. *Journal of Geophysical Research: Space Physics*, *127*(11), e2022JA030960. https://doi.org/10.1029/2022JA030960
Lin, D., Sorathia, K., Wang, W., Merkin, V., Bao, S., Pham, K., et al. (2021). The role of diffuse electron precipitation in the formation of subauroral polarization streams. *Journal of Geophysical Research: Space Physics*, *126*(12), e29792. https://doi.org/10.1029/2021JA029792
Lyons, L. R., Nishimura, Y., Zhang, S., Coster, A., Liu, J., Bristow, W. A., et al. (2021). Direct connection between auroral oval streamers/flow channels and equatorward traveling ionospheric disturbances. *Frontiers in Astronomy and Space Sciences*, *8*, 169. https://doi.org/10.3389/fspas.2021.738507
Main, D., & Sotnikov, V. (2020). Parametric interaction between ELF and VLF waves: 3D LSP simulation results. *Physics of Plasmas*, *27*(2), 022304. https://doi.org/10.1063/1.5126675
Malaspina, D. M., Andersson, L., Ergun, R. E., Wygant, J. R., Bonnell, J. W., Kletzing, C., et al. (2014). Nonlinear electric field structures in the inner magnetosphere. *Geophysical Research Letters*, *41*(16), 5693–5701. https://doi.org/10.1002/2014GL061109
McFadden, J. P., Carlson, C. W., Larson, D., Ludlam, M., Abiad, R., Elliott, B., et al. (2008). The THEMIS ESA plasma instrument and in-flight calibration. *Space Science Reviews*, *141*(1–4), 277–302. https://doi.org/10.1007/s11214-008-9440-2
Mishin, E. V. (2013). Interaction of substorm injections with the subauroral geospace: 1. Multispacecraft observations of SAID. *Journal of Geophysical Research: Space Physics*, *118*(9), 5782–5796. https://doi.org/10.1002/jgra.50548
Mishin, E. V. (2023). The evolving paradigm of the subauroral geospace. *Frontiers in Astronomy and Space Sciences*, *10*. https://doi.org/10.3389/fspas.2023.1118758
Mishin, E. V., Albert, J., & Santolik, O. (2011). SAID/SAPS-related VLF waves and the outer radiation belt boundary. *Geophysical Research Letters*, *38*(21), L21101. https://doi.org/10.1029/2011GL049613
Mishin, E. V., Nishimura, Y., & Foster, J. (2017). SAPS/SAID revisited: A causal relation to the substorm current wedge. *Journal of Geophysical Research: Space Physics*, *122*(8), 8516–8535. https://doi.org/10.1002/2017JA024263

Mishin, E. V., & Sotnikov, V. (2017). The turbulent plasmasphere boundary layer and the outer radiation belt boundary. *Plasma Physics and Controlled Fusion*, *59*(12), 124003. https://doi.org/10.1088/1361-6587/aa8481

Mishin, E. V., Sotnikov, V., Gershenzon, N., & Sharma, A. (2019). Whistler waves in the plasmasphere boundary layer: Nonlinear parametric excitation. *Geophysical Research Letters*, *46*(13), 7131–7136. https://doi.org/10.1029/2019GL083432

Mishin, E. V., & Streltsov, A. (2021). Mesoscale and small-scale structure of the subauroral geospace. In C. Huang & G. Lu (Eds.), *Ionosphere dynamics and applications* (Vol. 3, p. 139). https://doi.org/10.1002/9781119815617.ch8

Miyoshi, Y., Hori, T., Shoji, M., Teramoto, M., Chang, T. F., Segawa, T., et al. (2018). The ERG Science Center. *Earth Planets and Space*, *70*(1), 96. https://doi.org/10.1186/s40623-018-0867-8

Miyoshi, Y., Hosokawa, S., Kurita, S.-I., Oyama, Y., Ogawa, S., Saito, I., et al. (2021). Penetration of MeV electrons into the mesosphere accompanying pulsating aurorae. *Scientific Reports*, *11*(1), 13724. https://doi.org/10.1038/s41598-021-92611-3

Miyoshi, Y., Kasaba, Y., Shinohara, I., Takashima, T., Asamura, K., Matsumoto, H., et al. (2017). Geospace exploration project: Arase (ERG). *Journal of Physics: Conference Series*, *869*, 012095. https://doi.org/10.1088/1742-6596/869/1/012095

Moffett, R. J., Ennis, A. E., Bailey, G. J., Heelis, R. A., & Brace, L. H. (1998). Electron temperatures during rapid subauroral ion drift events. *Annales Geophysicae*, *16*(4), 450–459. https://doi.org/10.1007/s00585-998-0450-x

Newell, P. T., Sergeev, V. A., Bikkuzina, G. R., & Wing, S. (1998). Characterizing the state of the magnetosphere: Testing the ion precipitation maxima latitude (b2i) and the ion isotropy boundary. *Journal of Geophysical Research*, *103*(A3), 4739–4746. https://doi.org/10.1029/97JA03622

Nishimura, Y., Bortnik, J., Li, W., Thorne, R. M., Ni, B., Lyons, L. R., et al. (2013). Structures of dayside whistler-mode waves deduced from conjugate diffuse aurora. *Journal of Geophysical Research: Space Physics*, *118*(2), 664–673. https://doi.org/10.1029/2012JA018242

Nishimura, Y., Donovan, E. F., Angelopoulos, V., & Nishitani, N. (2020). Dynamics of auroral precipitation boundaries associated with STEVE and SAID. *Journal of Geophysical Research: Space Physics*, *125*(8), e28067. https://doi.org/10.1029/2020JA028067

Nishimura, Y., Hussein, A., Erickson, P. J., Gallardo-Lacourt, B., & Angelopoulos, V. (2022). Statistical study of magnetospheric conditions for SAPS and SAID. *Geophysical Research Letters*, *49*(9), e98469. https://doi.org/10.1029/2022GL098469

Ohma, A., Østgaard, N., Reistad, J. P., Tenfjord, P., Laundal, K. M., Snekvik, K., et al. (2018). Evolution of asymmetrically displaced footpoints during substorms. *Journal of Geophysical Research: Space Physics*, *123*(12), 10030–10063. https://doi.org/10.1029/2018JA025869

Oyama, S., Kero, A., Rodger, C. J., Clilverd, M. A., Miyoshi, Y., Partamies, N., et al. (2017). Energetic electron precipitation and auroral morphology at the substorm recovery phase. *Journal of Geophysical Research: Space Physics*, *122*(6), 6508–6527. https://doi.org/10.1002/2016JA023484

Pettit, J., Elliott, S., Randall, C., Halford, A., Jaynes, A., & Garcia-Sage, K. (2023). Investigation of the drivers and atmospheric impacts of energetic electron precipitation. *Frontiers in Astronomy and Space Sciences*, *10*, 1162564. https://doi.org/10.3389/fspas.2023.1162564

Puhl-Quinn, P. A., Matsui, H., Mishin, E., Mouikis, C., Kistler, L., Khotyaintsev, Y., et al. (2007). Cluster and DMSP observations of SAID electric fields. *Journal of Geophysical Research*, *112*(A5), A05219. https://doi.org/10.1029/2006JA012065

Rich, F. J., & Hairston, M. (1994). Large-scale convection patterns observed by DMSP. *Journal of Geophysical Research*, *99*(A3), 3827–3844. https://doi.org/10.1029/93JA03296

Rideout, W., & Coster, A. (2006). Automated GPS processing for global total electron content data. *GPS Solutions*, *10*(3), 219–228. https://doi.org/10.1007/s10291-006-0029-5

Rodger, A. (2008). The mid-latitude trough—Revisited. *Washington DC American Geophysical Union Geophysical Monograph Series*, *181*, 25–33. https://doi.org/10.1029/181GM04

Sergeev, V. A., Malkov, M., & Mursula, K. (1993). Testing the isotropic boundary algorithm method to evaluate the magnetic field configuration in the tail. *Journal of Geophysical Research*, *98*(A5), 7609–7620. https://doi.org/10.1029/92JA02587

Sergeev, V. A., Nishimura, Y., Kubyshkina, M., Angelopoulos, V., Nakamura, R., & Singer, H. (2012). Magnetospheric location of the equatorward prebreakup arc. *Journal of Geophysical Research: Space Physics*, *117*(A1), A01212. https://doi.org/10.1029/2011JA017154

Sheng, C., Deng, Y., Chen, Y.-J., Heelis, R. A., & Huang, Y. (2019). Effects of alignment between particle precipitation and ion convection patterns on Joule heating. *Journal of Geophysical Research: Space Physics*, *124*(6), 4905–4915. https://doi.org/10.1029/2018JA026446

Sheng, C., Deng, Y., Gabrielse, C., Lyons, L. R., Nishimura, Y., Heelis, R. A., & Chen, Y.-J. (2021). Sensitivity of upper atmosphere to different characteristics of flow bursts in the auroral zone. *Journal of Geophysical Research: Space Physics*, *126*(10), e29253. https://doi.org/10.1029/2021JA029253

Shiokawa, K., Anderson, R., Daglis, I., Hughes, W., & Wygant, J. (1999). Simultaneous DMSP and CRRES observation of broadband electrons during a storm-time substorm on March 25, 1991. *Physics and Chemistry of the Earth C*, *24*(1–3), 281–285. https://doi.org/10.1016/S1464-1917(98)00040-3

SPEDAS. (2023). Space physics environment data analysis software [Software]. SPEDAS. Retrieved from http://spedas.org/wiki/index.php?title=Downloads_and_Installation

Spiro, R. W., Heelis, R. A., & Hanson, W. B. (1979). Rapid subauroral ion drifts observed by Atmosphere Explorer C. *Geophysical Research Letters*, *6*(8), 657–660. https://doi.org/10.1029/GL006i008p00657

Streltsov, A. V., & Mishin, E. V. (2020). ULF waves generated near the plasmapause by the magnetosphere-ionosphere interactions. *Journal of Geophysical Research: Space Physics*, *125*(2), e27353. https://doi.org/10.1029/2019JA027353

TEC. (2023). Madrigal database of total electron content (TEC) [Dataset]. TEC. Retrieved from http://cedar.openmadrigal.org

Tian, X., Yu, Y., Gong, F., Ma, L., Cao, J., Solomon, S. C., et al. (2023). Ionospheric modulation by EMIC wave-driven proton precipitation: Observations and simulations. *Journal of Geophysical Research: Space Physics*, *128*(1), e2022JA030983. https://doi.org/10.1029/2022JA030983

Tsai, E., Artemyev, A., Zhang, X.-J., & Angelopoulos, V. (2022). Relativistic electron precipitation driven by nonlinear resonance with whistler-mode waves. *Journal of Geophysical Research: Space Physics*, *127*(5), e30338. https://doi.org/10.1029/2022JA030338

Vierinen, J., Coster, A. J., Rideout, W. C., Erickson, P. J., & Norberg, J. (2015). Statistical framework for estimating GNSS bias. *Atmospheric Measurement Techniques Discussions*, *8*(9), 9373–9398. https://doi.org/10.5194/amtd-8-9373-2015

Vo, H. B., & Foster, J. C. (2001). A quantitative study of ionospheric density gradients at midlatitudes. *Journal of Geophysical Research*, *106*(A10), 21555–21564. https://doi.org/10.1029/2000JA000397

Wang, W., Yang, J., Nishimura, Y., Sun, W., Wei, D., Zhang, F., et al. (2021). Magnetospheric source and electric current system associated with intense SAIDs. *Geophysical Research Letters*, *48*(22), e93253. https://doi.org/10.1029/2021GL093253

Wang, Z., Zou, S., Shepherd, S. G., Liang, J., Gjerloev, J. W., Ruohoniemi, J. M., et al. (2019). Multi-instrument observations of mesoscale enhancement of subauroral polarization stream associated with an injection. *Journal of Geophysical Research: Space Physics*, *124*(3), 1770–1784. https://doi.org/10.1029/2019JA026535

Wilkins, C., Angelopoulos, V., Runov, A., Artemyev, A., Zhang, X. J., Liu, J., & Tsai, E. (2023). Statistical characteristics of the electron isotropy boundary. *Journal of Geophysical Research: Space Physics*, *128*(10), e2023JA031774. https://doi.org/10.1029/2023JA031774

Xu, W., Marshall, R. A., Tyssøy, H. N., & Fang, X. (2020). A generalized method for calculating atmospheric ionization by energetic electron precipitation. *Journal of Geophysical Research: Space Physics*, *125*(11), e28482. https://doi.org/10.1029/2020JA028482

Yahnin, A., & Yahnina, T. (2007). Energetic proton precipitation related to ion cyclotron waves. *Journal of Atmospheric and Solar-Terrestrial Physics*, *69*(14), 1690–1706. https://doi.org/10.1016/j.jastp.2007.02.010

Yahnin, A. G., Yahnina, T. A., Semenova, N. V., Gvozdevsky, B. B., & Pashin, A. B. (2016). Relativistic electron precipitation as seen by NOAA POES. *Journal of Geophysical Research: Space Physics*, *121*(9), 8286–8299. https://doi.org/10.1002/2016JA022765

Yizengaw, E., & Moldwin, M. B. (2005). The altitude extension of the mid-latitude trough and its correlation with plasmapause position. *Geophysical Research Letters*, *32*(9), L09105. https://doi.org/10.1029/2005GL022854

Yu, Y., Cao, J., Pu, Z., Jordanova, V. K., & Ridley, A. (2022). Meso-scale electrodynamic coupling of the Earth magnetosphere-ionosphere system. *Space Science Reviews*, *218*(8), 74. https://doi.org/10.1007/s11214-022-00940-0

Yu, Y., Jordanova, V. K., McGranaghan, R. M., & Solomon, S. C. (2018). Self-consistent modeling of electron precipitation and responses in the ionosphere: Application to low-altitude energization during substorms. *Geophysical Research Letters*, *45*(13), 6371–6381. https://doi.org/10.1029/2018GL078828

Zhang, X.-J., Angelopoulos, V., Artemyev, A., Mourenas, D., Agapitov, O., Tsai, E., & Wilkins, C. (2023). Temporal scales of electron precipitation driven by whistler-mode waves. *Journal of Geophysical Research: Space Physics*, *128*(1), e2022JA031087. https://doi.org/10.1029/2022JA031087

Zhang, X.-J., Angelopoulos, V., Mourenas, D., Artemyev, A., Tsai, E., & Wilkins, C. (2022). Characteristics of electron microburst precipitation based on high-resolution ELFIN measurements. *Journal of Geophysical Research: Space Physics*, *127*(5), e30509. https://doi.org/10.1029/2022JA030509